3D Electron Diffraction as GIWAXS Alternative for Quantitative Structural Characterization of Organic Solar Cells

Irene Kraus[1], Mingjian Wu[1], Stefanie Rechberger[1], Johannes Will[1], Santanu Maiti[2], Andreas Kuhlmann[3,4,5], Marten Huck[3,4,5], Larry Lüer[6,7], Florian Bertram[8], Hans-Georg Steinrück[3,4,5], Tobias Unruh[2], Christoph J. Brabec[6,7] and Erdmann Spiecker[1]*

[1] Institute of Micro- and Nanostructure Research & Center for Nanoanalysis and Electron Microscpy (CENEM) Friedrich-Alexander-Universität Erlangen-Nürnberg, IZNF, Cauerstraße 3, 91058 Erlangen, Germany

[2] Institute for Crystallography and Structural Physics, Friedrich-Alexander-Universität Erlangen-Nürnberg, Staudtstraße 3, 91058 Erlangen, Germany

[3] Institute for a Sustainable Hydrogen Economy (INW), Forschungszentrum Jülich GmbH, Marie-Curie-Straße 5, 52428 Jülich, Germany

[4] Institute of Physical Chemistry, RWTH Aachen University, Landoltweg 2, 52074 Aachen, Germany

[5] Department of Chemistry, Paderborn University, Warburger Straße 100, 33098 Paderborn, Germany

[6] Institute Materials for Electronics and Energy Technology (iMEET), Friedrich-Alexander-Universität Erlangen-Nürnberg, Martensstraße 7, 91058 Erlangen, Germany

[7] Helmholtz Institute Erlangen-Nürnberg for Renewable Energy (HIERN), Forschungszentrum Jülich GmbH, 91058 Erlangen, Germany

[8] Deutsches Elektronen-Synchrotron DESY, Notkestraße 85, 22607 Hamburg, Germany

*Corresponding author: erdmann.spiecker@fau.de

Abstract

We demonstrate elastically filtered 3D Electron Diffraction (3D ED) as a powerful alternative technique to Grazing Incidence Wide-Angle X-ray Scattering (GIWAXS) for quantitatively characterizing the structure of organic semiconductor films. Using a model material system of solvent vapor annealed $DRCN5T:PC_{71}BM$ thin film, which is employed in organic solar cells (OSCs), we extract the structural data obtained from 3D ED and compare with that from GIWAXS, utilizing both laboratory and synchrotron X-ray sources. Quantitative evaluation of the datasets in terms of peak positions, peak widths and mosaicity revealed good agreement between both techniques, qualifying 3D ED as an alternative tool for analyzing highly beam-sensitive organic thin films. Furthermore, the respective advantages and limitations of 3D ED and GIWAXS are discussed, emphasizing the unique capability of 3D ED to integrate seamlessly with the diverse imaging and spectroscopic modalities in modern TEM. This integration enriches the techniques of structural characterization of OSCs, paving the way for deeper insights into their structural properties and ultimately their performance.

1. Introduction

Organic solar cells (OSCs) have seen remarkable advancements in recent years, with power conversion efficiencies now exceeding 20%[1,2], largely driven by innovations in molecular design[2-6], material engineering and processing optimization[7-13]. The most widely studied OSCs are bulk-heterojunction (BHJ) solar cells, where donor and acceptor materials are intimately blended at the nanoscale to facilitate efficient charge generation and transport. The performance of these devices is inherently linked to their structural organization and nanomorphology, as the molecular assembly and ordering dictate efficiencies of the primary processes in OCS (light absorption, exciton dissociation, charge separation, charge collection) with often contradicting requirements: for example, large domains facilitate charge collection but limit exciton dissociation. The contradiction is alleviated by domains of high anisotropy, showing efficient exciton dissociation and charge collection at the same time[14]. This example shows that detailed knowledge of nanoscopic structure is needed to understand optoelectronic performance. Moreover, the structural evolution of OSCs is highly sensitive to processing conditions, with parameters such as solvent choice, annealing, and deposition techniques critically influencing the resulting morphology.[8,15,16] Given the strong structure-property relationship in OSCs, precise characterization of their molecular organization and nanoscale morphology is essential for understanding and optimizing device performance.

Grazing-Incidence Wide-Angle X-ray Scattering (GIWAXS) is an established and widely used technique for quantitatively characterizing the structure of OSCs, utilizing both laboratory and synchrotron X-ray sources. From GIWAXS measurements, one can extract key structural parameters, including molecular packing distances, crystallite size, degree of orientation, and phase purity,[17-19] all of which are crucial for understanding structure-property relationships in OSCs. By leveraging the in-plane isotropy of bulk-heterojunction OSCs, GIWAXS provides simultaneous access to both in-plane and out-of-plane structural information in a single measurement, offering critical insights into molecular packing and orientation— key factors governing charge transport. Additionally, GIWAXS can be performed under various environmental conditions, enabling in situ studies of structural evolution during thermal annealing or solvent vapor annealing.[20] However, while GIWAXS effectively captures ensemble-averaged structural information, it does not provide real-space images of nanomorphology or local structural heterogeneities. This limitation motivates the exploration of complementary techniques, such as electron diffraction and electron microscopy, to gain deeper insight into the nanoscale structure of OSCs.

The scattering of X-rays and fast electrons is closely related. While X-rays interact with the local electron density of the atoms in the target material,[18] fast electrons are scattered by the electrostatic potential generated by the positively charged nuclei and screened by the surrounding electrons.[21] Using the Poisson equation, the atomic scattering factors for X-rays and electrons can be directly converted into each other, as described by the Mott formula.[22] Moreover, diffraction of both X-rays and fast electrons in crystalline materials follows the same fundamental principles, governed by Bragg's law.[21] Thus, in principle, both probes can provide equivalent structural information. Transmission electron microscopy (TEM) offers several distinct advantages for the structural characterization of thin-film materials, including OSCs. Modern TEM optics enable structural analysis across multiple length scales, from large-area parallel illumination (tens to hundreds of micrometers) to atomic-resolution imaging with aberration-corrected probes. TEM also allows seamless switching between diffraction and imaging modes, capturing structural information in both reciprocal and real space. In addition to diffraction and imaging, TEM provides access to analytical signals typically via inelastically scattered electrons and/or emitted characteristic X-rays, which are highly valuable for mapping the distribution of elements, enabling direct visualization of donor-acceptor intermixing and phase separation in OSCs when sufficient chemical contrast is present. For example, Carbon, Sulfur, Nitrogen, or Oxygen signals can serve as fingerprints to distinguish different molecular components in various binary and even ternary BHJs.[8,9,16,23-27] However, a key challenge in using TEM for OSCs is radiation damage, as organic materials are highly beam-sensitive, requiring careful optimization of electron dose to preserve structural integrity. Additionally, while the transmission

geometry of TEM naturally provides high-resolution in-plane structural information, probing out-of-plane information necessitates sample tilting, i.e., different projections. Alternatively, TEM investigations can be conducted in cross-sectional geometry; however, this approach requires intricate focused ion beam (FIB) preparation. While successfully implemented[9], FIB preparation introduces significant ion beam damage and limits the sample area that can be studied compared to plan-view analysis. Electron diffraction in TEM is a highly versatile and dose-efficient technique to obtain structural insights of samples under investigation. Among its modalities, 3D Electron Diffraction (3D ED) has emerged as a powerful tool for mapping three-dimensional reciprocal space with high accuracy and precision. Originally developed for the structural analysis of submicron-sized crystals that are too small for conventional single-crystal X-ray diffraction, 3D ED has proven to be a transformative technique in crystallography. Landmark developments, including several automated data acquisition approaches[28-32] and *ab initio* structure determination routines[33-35], have enabled the automated workflows and precise determination of crystal structures, even for complex and beam-sensitive materials ranging from metal-organic frameworks, pharmaceutical compounds, and complex minerals, solidifying its place as a key tool in modern crystallography.[36] Despite these successes, 3D ED has not yet been widely adopted for studying the structure of polycrystalline and partially ordered materials, and within the OSC research community, its potential remains largely unexplored. This limited use can be attributed to several challenges: (1) the strong inelastic scattering in OSCs necessitates elastic filtering, which is not always available, and (2) the high sensitivity of OSCs to electron irradiation requires careful optimization of experimental conditions to mitigate beam-induced damage. However, these challenges do not pose fundamental limitations, and with appropriate advancements in experimental setups and methodologies, 3D ED has the potential to provide novel structural insights into OSCs.

In this study, we demonstrate the use of 3D ED as a quantitative technique for the structural characterization of polycrystalline organic thin films. Using a model BHJ system consisting of the small-molecule donor DRCN5T and the fullerene acceptor $PC_{71}BM$ that have been extensively studied,[8,15,16,37,38] we compare the structural information obtained from 3D ED with that from GIWAXS, using both laboratory and synchrotron X-ray sources. We present a comprehensive experimental workflow that covers sample preparation, data acquisition, stitching, and reduction. Our results show strong agreement between 3D ED and GIWAXS, confirming the reliability of 3D ED for structural analysis of OSCs. We also discuss the strengths and limitations of both techniques and highlight the potential for integrating 3D ED with other TEM-based methods to enhance the characterization of OSCs.

2. 3D ED and GIWAXS

2.1 Diffraction Geometry

We begin by briefly describing the scattering geometries of 3D ED and GIWAXS to facilitate clearer comparisons and discussions in subsequent sections. **Figure 1** a-c schematically illustrates the typical measurement setups of GIWAXS, plan-view ED and 3D ED, respectively. In GIWAXS, an X-ray beam, characterized by its wavevector $\mathbf{k}_{i,GIWAXS}$, impinges on the sample at a low incidence angle $\alpha_{i,GIWAXS}$. For thin films coated on substrates, using low incidence angles enables forward scattering, allowing a 2D detector placed in the far field to record the scattered signals. These signals are typically expressed in terms of their momentum transfer components, which are parallel (in-plane) and perpendicular (out-of-plane) to the thin film surface. The grazing incidence geometry results in an extended footprint on the sample surface, which can contribute to peak broadening,[18,39,40] as discussed later in more detail. For films on substrates, the incidence angle is typically chosen relative to the critical angles of total external reflection α_c of both substrate and film. The critical angle of the film is determined only by the electron density for a specific X-ray wavelength.

In Figure 1a an exemplary diffraction pattern of a polycrystalline sample is displayed. Each point in the detector plane is characterized by a specific exit wavevector $\mathbf{k}_{f,GIWAXS}$, which is represented by the out-of-plane and in-plane diffraction angles $\alpha_{f,GIWAXS}$ and θ_f. Within the OSC-community, crystallite orientations are commonly described in terms of the orientation of the molecular π-π stacking relative to the substrate. When the π-π stacking direction is either perpendicular or parallel to the substrate surface, the molecular orientations are referred to as face-on or edge-on, respectively.[38,41] Due to the finite incidence angle in GIWAXS, exact in-plane information, in particular relevant for edge-on crystallites, is not accessible; therefore, the crystallite in Figure 1a is depicted as slightly inclined.

Figure 1b shows a typical plan-view setup for electron diffraction in the TEM. In this configuration, the electron beam propagates through the sample with the wave vector of the incident beam $\mathbf{k}_{i,TEM}$ oriented perpendicular to the film. Due to the high electron energies in TEM, the wave vector is nearly two orders of magnitude longer than in GIWAXS, resulting in extremely small Bragg angles, much less than 1° for typical lattice plane spacings in organic crystals. Consequently, the Bragg condition is only fulfilled for lattice planes oriented nearly parallel to the incident electron beam, i.e. the electron beam hits the lattice planes edge-on. An example crystallite with edge-on π-π stacking is shown in Figure 1b. Due to the random in-plane orientation of the crystals, this results in a diffraction ring with radius determined by the Bragg-

angle. For better illustration, the diffraction geometry is not shown to scale in Figure 1b and 1c. In reality, the diffraction vector $\mathbf{k}_{f,TEM}$ is almost parallel to $\mathbf{k}_{i,TEM}$, the angle between the two vectors being two times the Bragg angle (<< 1°).

The versatile electron optics of the TEM allows for flexible adjustment of the diffraction pattern and enables other techniques to be combined with electron diffraction. Firstly, the variable camera length enables magnification (or demagnification) the diffraction pattern over a wide range. This allows the reciprocal lattice area (or $\mathbf{q}$-space) covered by the detector, the sampling of the $\mathbf{q}$-space and the signal-to-noise ratio (SNR) to be flexibly adjusted to meet specific sample requirements. Secondly, to obtain a diffraction pattern from a specific sample area, a so-called selected area electron diffraction (SAED) pattern, a selected area diffraction (SAD) aperture can be inserted in the first image plane of the microscope (not shown). Finally, if an imaging energy filter is available, an energy selection slit can be inserted in the energy dispersive plane of the filter to produce an elastic energy filtered selected area electron diffraction (EF-SAED) pattern.[21] Energy filtering is essential to suppress the pronounced inelastic scattering background at small scattering angles, thus improving the signal-to-background ratio (SBR) in scattering regions relevant to organic crystals with large unit cells (on the nm scale).

In TEM, different incidence angles of the electron beam on the sample can be achieved by tilting the sample relative to the incident beam (**Figure 1**c). The tilt angle α_{TEM} is defined with respect to the goniometer tilt axis of the specimen holder, with plan-view specified as $\alpha_{TEM}=0°$. Recording diffraction patterns over a range of sample tilt angles with discrete tilt steps allows to probe the reciprocal space in three dimensions, as explained in a later paragraph in this section in more detail. For related techniques and acquisition procedures different names can be found in literature, but can be summarised under the term 3D ED.[36,42] The resulting series composed of diffraction patterns recorded at different incidence angles is hereafter referred to as a tilt series.

Comparing the commonly used definitions of incidence angles in TEM and GIWAXS results in the following relationship:

$\alpha_{TEM}=90°- \alpha_{i,GIWAXS}$.

Additionally, the scaling of vectors in reciprocal space, including wavevectors $\mathbf{k}$, diffraction vectors $\mathbf{q} = \mathbf{k}_f - \mathbf{k}_i$ and reciprocal lattice vectors $\mathbf{g}$, differ by a factor of 2π when comparing standard notations in electron and X-ray diffraction.[41,43] In this work, we apply the notations commonly used in ED consistently to both

6

3D ED and GIWAXS data to allow for a straightforward comparison. In the ED notation, $|\mathbf{g}|=1/d$ and $|\mathbf{k}|=1/\lambda$, which is particularly convenient, as the interplanar lattice spacing d and the wavelength λ can be directly calculated from $|\mathbf{g}|$ and $|\mathbf{k}|$ through simple inversion.
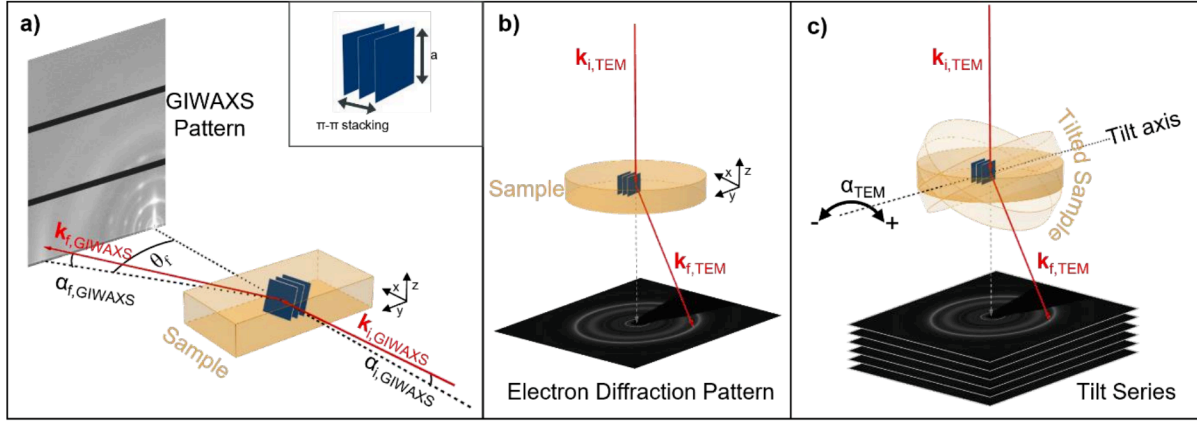
Figure 1. Schematic comparison of scattering geometries of GIWAXS and ED. a) In GIWAXS the incident X-rays impinge on the sample under an grazing angle $\alpha_{i,GIWAXS}$ and the diffracted signal is detected by a detector perpendicular to the sample plane. The inset illustrates crystallites of characteristic lattice distances, lamellar packing a (on the order of ~2nm) and perpendicular π-π stacking (on the order 0.3-0.4 nm). b) Plan-view electron diffraction in the TEM, in contrast, uses an electron beam being transmitted through the sample perpendicular to the sample plane, with detection of the diffraction pattern below the sample. c) By tilting the sample around the specified tilt axis, defined by the sample holder, different incidence angles of the electron beam on the sample are achieved, enabling the acquisition of a tilt series.
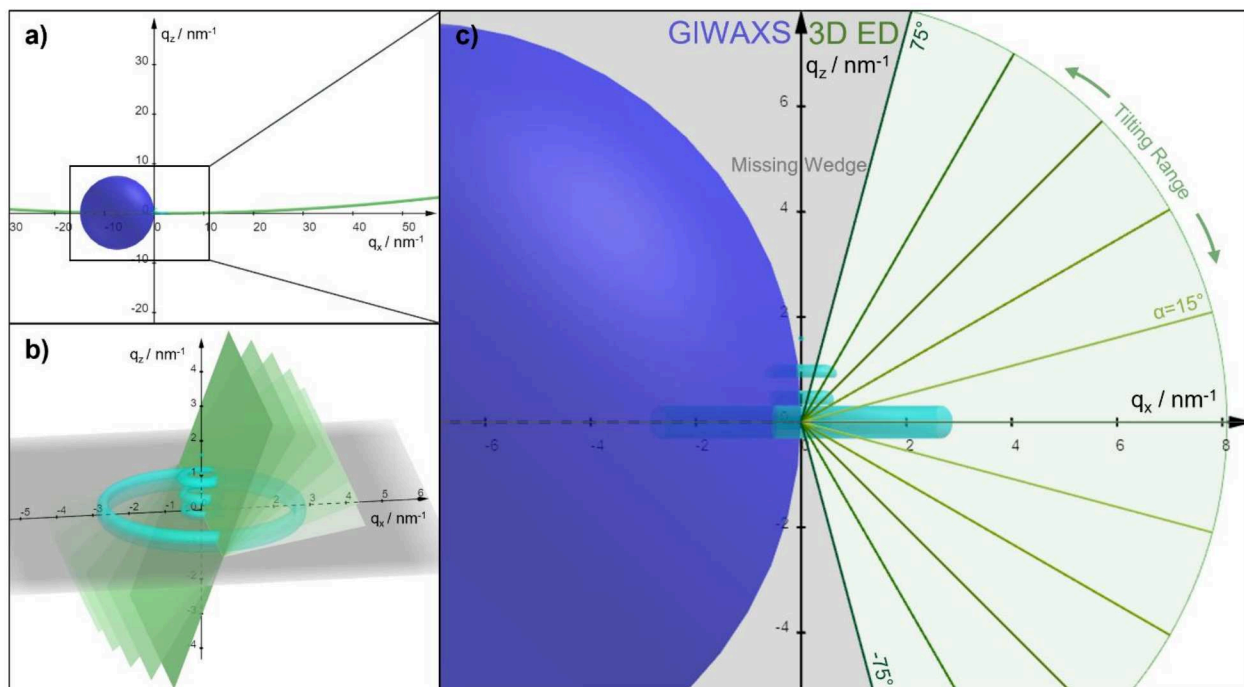
2.2 Reciprocal Space Sampling

Diffraction experiments can be understood as a sectioning (and consequently sampling) of the reciprocal space – defined by the coordinates q_x, q_y in-plane and q_z out-of-plane- using the Ewald sphere, as described by the Ewald sphere construction.[44,45] **Figure 2** illustrates the reciprocal space sampling of 3D ED and GIWAXS using a schematic reciprocal space representation of an OSC absorber film having a fiber texture, i.e., dominant edge-on π-π stacking, while the crystallites have random in-plane orientation. For simplicity, only a few features of the reciprocal space are depicted. The large and with respect to the q_z-axis symmetric turquoise ring in the q_{xy} plane represents the **g** vectors of crystallites with π-π stacking in edge-on orientation, characterized by a typical d spacing of 3.6 Å. The turquoise dots along the z-axis and the small turquoise rings correspond to lattice planes with significantly larger d spacings, typically associated with lamellar stacking, backbone stacking, or a combination thereof. To illustrate the sectioning by the Ewald spheres, only a few rings are shown as examples. To account for some mosaicity, i.e. variation in the orientation of the textured film, all features are broadened.

As the radius of the Ewald sphere corresponds to the length of the wave vector $|\mathbf{k}|$, there is an inverse relationship between the size of the Ewald sphere and the wavelength of the scattering probe. Due to the different wavelengths of electrons and X-rays in 3D ED and GIWAXS respectively, the sizes of the Ewald spheres differ as illustrated in **Figure 2**a: the extremely short wavelength $\lambda_{ED,300kV}$=0.00197 nm of electrons with kinetic energy of 300 keV, i.e. accelerated by a typical acceleration voltage of 300 kV, results in a relatively large Ewald sphere with a radius of $|\mathbf{k}|$=507.95 nm^{-1}, in contrast to the comparably small $|\mathbf{k}|$=6.49 nm^{-1} for X-rays with $\lambda_{Cu,K\alpha}$=0.154 nm for a standard Cu K$_\alpha$ source. Since the Ewald sphere size determines the curvature of the reciprocal space cut, an approximation of this cut as flat is reasonable and commonly done for 3D ED.[28,46] Within this approximation, the electron diffraction pattern on the detector directly reveals a flat section through the reciprocal lattice perpendicular to the incident wave vector $\mathbf{k}_i$. In contrast, for GIWAXS the curvature of the smaller Ewald sphere cannot be neglected. Since the diffraction pattern is detected on a flat detector, it does not directly represent reciprocal space coordinates in a plane perpendicular to $\mathbf{k}_i$. However, the detected pattern can be converted to q_r-q_z coordinates, taking into account the three-dimensional character of the Ewald sphere-reciprocal space cut by combining the reciprocal in-plane coordinates q_x and q_y to a polar coordinate q_r.[18,47] This conversion reveals that the q_z-axis is not sampled as it seems in the originally detected pattern, but that there is a missing curved wedge centered around and widening along the q_z-axis (see supporting information, SI, Figure S1).

Comparing the reciprocal space sampling of ED and GIWAXS, the different incidence directions of the scattering probes result in different sections of the reciprocal space being probed. In GIWAXS, the grazing incidence setup samples a curved vertical sphere segment of the reciprocal space, while in plan-view ED, i.e. for α_{TEM}=0°, the transmission geometry samples a horizontal planar cut through the reciprocal space, corresponding to the q_{xy} plane. In 3D ED, tilting the sample in real space and recording diffraction patterns at different tilt angles allows the sampling of different planes of reciprocal space, as shown in **Figure 2**b. The sampled reciprocal planes are tilted according to the tilt angle of the sample, with a common tilt axis in the q_{xy} plane. This technique thus allows three-dimensional sampling of the reciprocal space. However, the limited tilt range of the TEM stage (approximately ±75 to 80°) results in a wedge of missing information along the q_z-axis. **Figure 2**c compares the reciprocal space sampling of 3D ED and GIWAXS, highlighting the missing wedges for both methods, which arise for different reasons (see above). The comparison shows that the parts of the reciprocal space sampled by 3D ED and GIWAXS are quite similar, qualifying both as alternative methodologies for analyzing the crystal structure and texture of thin polycrystalline films. Due to the different shapes of the missing wedges – straight in 3D ED and curved in GIWAXS – GIWAXS provides more information near the q_z-axis for smaller values of q_z, while 3D ED excels at larger q_z. We note that for

both methods techniques and workflows are available to access the missing wedges, namely incidence angle series for GIWAXS[48] and cross-section sample preparation for TEM.

Figure 2. Reciprocal space sampling of 3D ED and GIWAXS. a) The different wavelengths of electrons and X-rays result in a relatively large electron Ewald sphere (green) and a comparably small one for X-rays (blue). b) Approximating the electron Ewald sphere as flat and acquiring diffraction patterns for different sample tilt angles results in a three-dimensional volume of reciprocal space being sampled in 3D ED. The green planes represent the flat cuts through reciprocal space, the turquoise features schematically depict the reciprocal space of a fiber-textured OSC film. c) The comparison of 3D ED and GIWAXS reciprocal space sampling shows the missing wedges for both methods and that 3D ED includes reciprocal space information similar to GIWAXS.

3. Results

As revealed in our previous studies[8,15,16,37,38], the model material system DRCN5T:PC_{71}BM after solvent vapor annealing presents a two dimensional oblique crystal system where the small molecule crystals co-exist in face-on and edge-on orientations.[38] For clarity, the term "π-π stacking direction" refers the DRCN5T molecule π-conjugate plane normal, corresponding to the unit cell [010] direction, which is perpendicular to the lamellar packing directions [100] and [001]. [38]

The workflow for acquisition of 3D ED datasets is depicted in **Figure 3**. First, a tilt series of ED patterns from -78 to 80° with a step width of 1° is acquired (cf. video in SI for whole tilt series). Here, beam damage

is mitigated by shifting the sample to a previously unexposed sample area after each tilting step (cf. Methods section), whereas the SBR is optimized by filtering inelastically scattered electrons. The resulting diffraction patterns at 0, 15, 30 and 75° tilt angle already give an impression of the textured underlying reciprocal lattice of the OSC thin film prior to any processing: Here the 0° pattern gives access to in-plane information as the q_{xy} reciprocal space plane is sampled. It is characterized by diffraction rings with uniform azimuthal intensity distribution as typical for polycrystalline thin film samples with isotropic in-plane crystal orientations (also known as 2D powder or fiber texture).[49] At higher tilt angles, anisotropy along the diffraction rings appears (i.e. segments of different intensity), indicating preferred orientations of crystallites. As discussed below, the occurrence of diffraction rings, as well as the intensity distribution evolution upon tilting, stems from the co-existence of three fractions, namely, the two preferred orientations edge-on and face-on, as well as an isotropic fraction. In the 0° pattern the edge-on fraction results in the homogeneous and bright outer ring ($q=2.73$ nm^{-1}) stemming from the π-π stacking of the small molecule. Further, the lamellar stacking of the face-on fraction gives rise to an intense diffraction ring close to the beam stop at $q=0.53$ nm^{-1}.[38] At higher tilt angles, the π-π stacking ring shows a more and more pronounced segment along the q_y-axis which corresponds to the tilt axis. Thereby the q_y-axis probes in-plane information independently of the tilting angle and the intense segment stems from the π-π stacking of edge-on oriented crystallites. The present but weaker intensity along the π-π stacking ring at higher tilt angles corresponds to a small fraction of three-dimensionally isotropically oriented crystallites. In contrast, the face-on orientation would lead to an intense segment on the π-π stacking ring centered around the out-of-plane q_z direction for a tilt angle of 90°. Since the degree of alignment of the crystallites close to face-on orientation (mosaicity) is smaller as compared to the missing wedge, this intensity enhancement is not observable and the face-on fraction only contributes to the diffraction rings originating from the lamellar stacking. The above-described discussion underlines that taking diffraction patterns under more than one tilt angle provides insight into the texture of organic thin films, which was also recently reported by us for other OSC films.[26]

In a next step, the reciprocal space volume is reconstructed out of the diffraction pattern tilt series including intensity normalization for every diffraction pattern originating from a changing contributing scattering volume and absorption effects upon sample tilting (cf. Method section). **Figure 3**b shows the reconstructed volume in an orthoplane view, consisting of three orthogonal planes with q_x, q_y or q_z-axis as normal vector, respectively. Further representations of the reconstructed 3D ED volume can be found in the SI (Figure S2 and additionally provided videos in SI). The reciprocal space reconstruction is mainly characterized by the superposition of two fiber-textured reciprocal lattices (cf. Figure 2) stemming from

the edge- and face-on fractions of DRCN5T. For further evaluation and comparison to GIWAXS, the volume is azimuthally integrated around the q_z-axis, as indicated in **Figure 3**b. Note, this step largely enhances signal to noise ratio (SNR) but also integrates intensity contributions stemming from different sample locations due to the sample shifts applied between the acquisition of diffraction patterns in a tilt series (see above). In this way q_x and q_y are represented by the radial q_r coordinate, as often done for GIWAXS [50], and a q_{rz} map is generated, which corresponds to a sampling of reciprocal space similar to GIWAXS. It is important to note that, although this integration averages the diffraction information from all sample positions examined in the tilt series, the resulting averaged diffraction information is still localized compared to that obtained from GIWAXS (contributing sample area in μm^2 range in 3D ED vs mm^2 in GIWAXS).
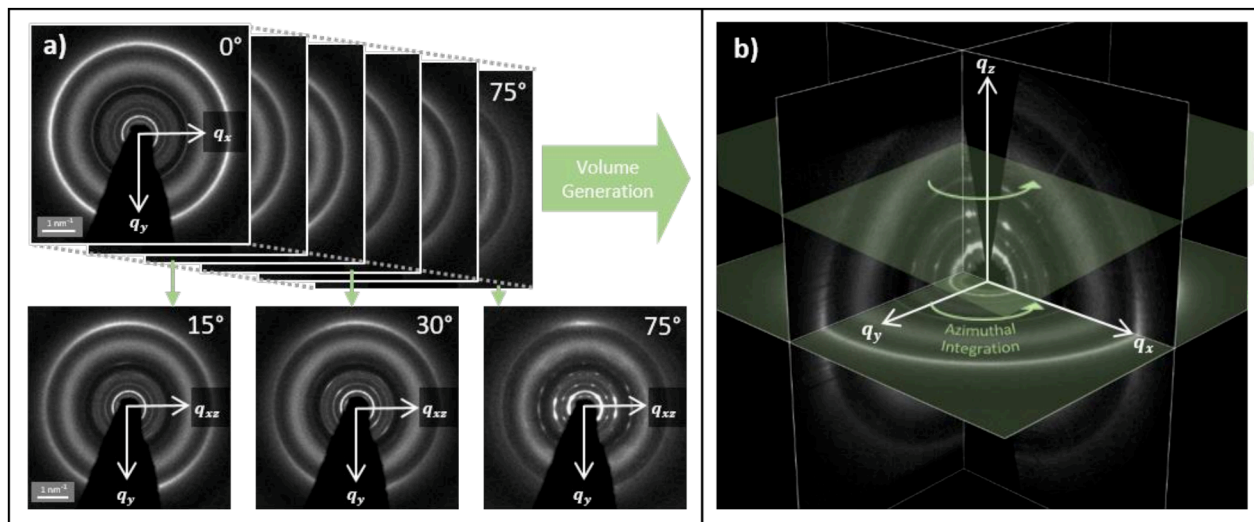
Figure 3. 3D ED processing workflow. a) A tilt series from -78 to 80° was acquired in 1° steps. Exemplary patterns at 0, 15, 30 and 75° sample tilt angle are shown indicating already the texture of the system by showing intense diffraction ring segments. b) Out of the tilt series the three-dimensional reciprocal space volume is reconstructed. For comparison to GIWAXS an azimuthal integration is performed.

For a first qualitative comparison, the reconstructed q_{rz} maps of 3D ED and GIWAXS are shown face-to-face, showcasing that the same diffraction rings and reflections are present and accessible with both techniques (see **Figure 4**a). This demonstrates the capability of 3D ED to gain correlative structural information as compared to GIWAXS. The good agreement of the q_{rz} maps allows indexing the occurring reflections based on GIWAXS data presented in literature from the same sample system.[38] While the amorphous halo around $q_r \approx 2$ nm^{-1} is related to $PC_{71}BM$, the sharper diffraction rings and their intense segments are present due to small molecule crystallites and their preferred orientations. For clarity only some reflections are indexed, a fully indexed version of the q_{rz} maps is shown in Figure S3. The displayed

q_{rz} maps also reveal the differently shaped missing wedges, which, as discussed above, originate from different causes in 3D ED and GIWAXS – limited tilt range in the former and the curved Ewald sphere in the latter.

For a more quantitative comparison of 3D ED and GIWAXS, different intensity profiles were extracted. Here, the GIWAXS in-plane information corresponds to the 0° ED pattern; their linecuts are compared in **Figure 4**b, quantitatively revealing excellent agreement. The better SNR of ED becomes apparent, even though the measurements were performed under low dose conditions to avoid beam damage. Additionally, as already mentioned, the 0° ED pattern represents the q_{xy} plane, providing direct insights into the in-plane crystal orientation distribution, which is isotropic in this case. In contrast, in GIWAXS, sample rotation around the axis normal to the sample surface would be required to capture potential anisotropic in-plane orientation of crystallites within the film. It should also be kept in mind that exact in-plane information is in GIWAXS only accessible in transmission geometry utilizing high-energy X-rays[51], otherwise, due to the experimental conditions, there is a shadowing effect of the sample horizon on the detector.[18] The horizontal cut is therefore extracted at a position displaced from q_z=0, in this case for a q_z range of 0.01 to 0.06 nm^{-1}. In consequence, for diffraction patterns comprised of rings (in contrast to rods) the diffraction peaks on the profile are slightly shifted towards lower q values and broadened, which may lead to a lower determined crystal coherence length (CCL). However, in the present case, those geometric effects are small and can be neglected (cf. Figure S4 and Table S1).

Based on the extracted in-plane profiles further quantification is carried out. The (100) peak, that refers to the lamellar stacking of the face-on fraction, and the (010) π-π stacking peak resulting from the edge-on fraction are analyzed in more detail. With the diffraction peak positions, their widths (full width half maximum, FWHM) and the wavelength of the respective probe, the CCL was calculated via the Scherrer equation using a shape factor of 1.[45] The results for both crystal orientations and both experimental methods are summarized in **Table 1** revealing the excellent quantitative agreement between both methods. In numbers a CCL of ~5 nm and ~20 nm is determined for the π-π stacking direction and the (100) direction, respectively. When assuming a similar lamellar stacking CCL for the edge-on fraction as determined for the face-on, those CCLs agree well with previous results of this material system and it's anisotropic leaf like morphology.[8]

In general, the CCLs should be treated with care when interpreting them as size of coherently scattering domains, as the peak width is not solely a function of crystal size, but inhomogeneity, strain and instrumental broadening also contribute.[18,49]

Table 1. CCLs were determined based on in-plane intensity profiles of 3D ED and GIWAXS for (100) and π-π stacking peak.
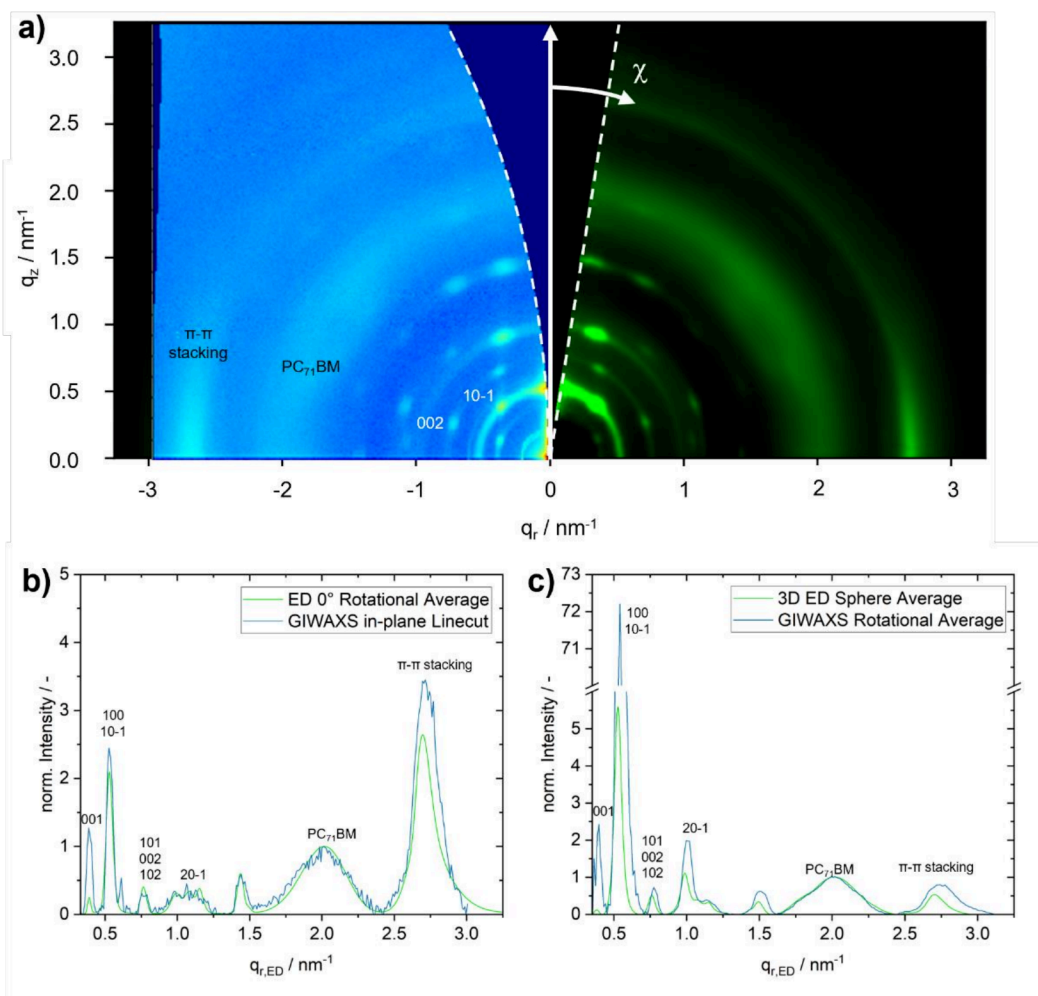
Method	3D ED	GIWAXS
(100) position / nm^{-1}	0.5307±0.0004	0.5325±0.0013
(100) FWHM / nm^{-1}	0.0532±0.0010	0.0470±0.0030
π-π position / nm^{-1}	2.7315±0.0029	2.7202±0.0038
π-π FWHM / nm^{-1}	0.1964±0.0051	0.1922±0.0099
CCL (100) / nm	18.80±0.35	21.26±1.34
CCL π-π / nm	5.09±0.13	5.20±0.27

In order to confirm the leaf like structure, additional STEM-EELS measurements were performed (cf. Figure S5) on the same sample, adding real space information to the 3D ED data by utilizing one strength of TEM investigations, which is fast switching from diffraction to imaging mode. Here, we utilized the Carbon and Sulfur ionization edges which reveal the distribution of the Carbon rich $PC_{71}BM$ and the sulfur containing DRCN5T, respectively. By comparing the size of the DRCN5T leaf like domains, with a long axis of about 79 nm and a short axis of ~33 nm, to the determined CCLs, it becomes apparent that one DRCN5T domain consists of multiple crystallites, further revealing the presence of grain boundaries as discussed in literature.[8]

Besides the in-plane cut, the intensity distribution in the q_{rz} maps can be rotationally averaged (see Figure 4c) to enhance the SNR and to fetch all scattering contributions beyond those contributing to the in-plane direction. Whereas in 3D ED this is straight forward, for GIWAXS reflection at the film-substrate interface and refraction at the film surface have been shown to split and shift peaks restricted to out-of-plane direction with no in-plane effect.[18,39] This in consequence leads to a virtual peak shift towards larger q values when simply taking rotational averages in GIWAXS. In order to compare the GIWAXS data and the 3D ED data, these effects were taken into account by rescaling the GIWAXS q_r scale by 1.5% (Figure S6). As the in-plane cuts, the resulting rotational averaged profiles show excellent agreement between the 3D ED and GIWAXS data.

Besides the correlative GIWAXS measurement performed at a laboratory source, we conducted additional experiments at P08 (DESY, Hamburg). As for the laboratory dataset, the synchrotron data reveals the excellent agreement between 3D ED and GIWAXS data (cf. Figure S7). Here, we however want to highlight

three aspects: i) the data acquisition after alignment at the synchrotron is significantly shorter (10 s vs. 16 h (laboratory source) vs. 3 h (3D ED)) enabling in situ investigations,[20,52] ii) the typically higher and tunable photon energy allows narrowing down the missing wedge of the GIWAXS data (cf. Figure S7c), nevertheless iii) the in-plane data, which shows a very good SNR ratio in 3D ED, is typically worse in GIWAXS. Whereas in 3D ED all crystallites of a fiber textured specimen contribute to the in-plane ring (0° tilt angle), only a very few crystallites contribute to the in-plane Bragg peaks in GIWAXS. This phenomenon is well-known in GIWAXS and taken into account by the $\sin(\chi)$ correction[18] for quantitative analysis.

Figure 4. Comparison of 3D ED and GIWAXS data. a) Qualitative overlay of 3D ED (right) and GIWAXS (left) q_{rz} reciprocal space maps with indexed peaks. Missing wedges along q_z-axis of both methods are marked by white dashed lines. A more quantitative comparison is based on different profiles extracted from the maps. b) A GIWAXS in-plane linecut corresponds to the 0° ED pattern rotationally averaged. In c) rotational averages of the q_{rz} maps from both methods are compared. All shown profiles are background subtracted and normalized with respect to the $PC_{71}BM$ peak.

Another quantity which can be extracted from the q_{rz} maps is the mosaicity, which refers to the degree of alignment of crystallites in an orientation. Here, the width of reflections is evaluated along an arc of constant q.[49] For this purpose, cuts along χ are extracted out of the q_{rz} maps, which is the angle between the substrate normal and the scattering vector (cf. Figure 4a). The results are summarized for different peaks in **Table 2**. Overall, the 3D ED and GIWAXS data are in very good agreement revealing a mosaicity of ~6° in both methods. The 3D ED (10-1) peak, however, exhibits a χ-width of about 8°. Due to geometric considerations the mosaicity of (002) and (10-1) peaks is related to each other and should be equal (cf. Figure S8a) as also documented by the GIWAXS data. A possible reason for the difference in 3D ED is local variations of the crystallite inclination, either due to sample inhomogeneity or buckling of the film on the TEM grid. Note, the sample is translated after each rotation step to mitigate beam damage in the 3D ED case, thus different positions contribute to the intensity distribution along the diffraction ring. In this context, buckling of the film supporting TEM transparent membrane[53,54] could lead to an apparent higher angular acceptance. Furthermore, the discrete tilting steps and the processing of the 3D ED q_{rz} map (cf. Method section) only allow an accuracy of 1° in the angular χ direction, which could in principle be improved by using finer tilting steps. We further evaluated the mosaicity of the in-plane π-π stacking peak, which refers to a different inclination axis for the crystallites (cf. Figure S8b). Here, both methods yield a similar value around ~22.5 °, again highlighting the correlative nature of 3D ED and GIWAXS.

Table 2. Comparison of peak positions and widths of χ-cuts extracted out of 3D ED and GIWAXS q_{rz} maps.

Method	3D ED	GIWAXS
(10-1) FWHM / °	8.12±0.06	6.33±0.33
(10-1) χ Position / °	40.86±0.03	40.81±0.14
(002) FWHM / °	6.84±0.11	6.35±0.36
(002) χ Position / °	69.32±0.04	68.77±0.12
In-plane π-π stacking FWHM / °	22.18±0.18	23.14±0.77

4. Discussion

The results above confirm that 3D ED is well-suited to provide structural information on highly beam sensitive OSC layers with a quality comparable to GIWAXS. However, it is evident that while both

15

techniques are complementary, each comes with its own challenges and strengths. This highlights the advantage of combining them for a more comprehensive structural characterization. In the following, we highlight the correlative character of the methods by first briefly discussing common challenges of both techniques, before we address their particular strengths and opportunities.

4.1. Challenges in 3D ED and GIWAXS

Since molecular semiconductors used in OSC layers are in general radiation-sensitive, the dose rate and cumulative dose which can be used are limited, which in turn limits the achievable SNR and thus quality of the data.[37] Due to the smaller illuminated area (μm^2 vs. mm^2) this challenge is typically affecting ED to a larger extend. Nevertheless, we demonstrated that energy filtering as well as moving to a fresh previously non-illuminated area in between each tilting step helps to significantly improve the SNR as well as mitigating beam damage. Beyond beam-sensitivity, accessing out-of-plane information is challenging in both techniques. Even though adjusting the X-ray energy and extending the tilt range, respectively, allow access to information near $q_r = 0$, obtaining pure q_z information remains challenging in both techniques. Achieving this requires additional measurements with varying X-ray incidence angles or dedicated preparation of cross-section TEM samples. Similarly, GIWAXS in reflection geometry also cannot access pure in-plane information due to the sample horizon and the finite incidence angle. Both challenges, though fundamentally present, are, however, not overly severe for OSC layers, due to their intrinsically broad mosaicity of several degrees,[55] as demonstrated for the DRC5NT system above. Other experimental challenges include instrumental broadening stemming from, e.g., the finite footprint in GIWAXS, or, as discussed above, refraction and reflection effects in GIWAXS, which lead to peak shifting and splitting in q_z direction. The latter can be theoretically calculated and, in principle, contain additional information about the sample, such as the refractive index and, in turn, the electron density. However, these effects have to be taken into account when determining the lattice parameters from a GIWAXS pattern.[39]

4.2. Strengths and Opportunities of 3D ED and GIWAXS

3D ED and GIWAXS are both capable of delivering spatially averaged (μm^2 to mm^2) and valuable structural information for beam sensitive OSC materials. Nevertheless, both techniques have their particular strengths, which qualifies them for specific objectives or their correlative use. In this context, GIWAXS stands out with the straight forward and facile sample preparation. Here, the functional thin film can be directly investigated after deposition on a support such as glass or silicon wafer. This, in combination with the short illumination times in particular at synchrotron sources enables in situ investigations even during

film formation or post-treatment such as solvent vapor annealing or thermal annealing. In addition, utilizing high-energy X-rays, as available at synchrotron sources, allows to mitigate beam damage and fill large portions of the missing wedge. Moreover, the GIWAXS setup is compatible with correlative methods such as X-ray reflectometry or photoluminescence, giving further insight into structural and electronical properties of the functional OSC thin film.[20] Other strengths of GIWAXS include the accessibility of z-dependent information within the OSC film by varying the incidence angle. So-called depth-profiling requires a highly collimated beam, realizable at a synchrotron source, and provides unique insight into the homogeneity of the film in the surface normal direction.[18] One recent development in GIWAXS involves the quantitative analysis of relative Bragg peak intensities to determine the positions of individual atoms within the crystal unit cell. Here, several factors such as Lorentz correction factors, absorptions effects, transmission coefficients, solid angle variations and even X-ray polarization effects have to be taken into account.[47] This is in principle also possible for 3D ED, as documented for single crystalline materials.[56,57] However, the theoretical workflow still needs to be established for polycrystalline materials such as functional OSC thin films. On the other hand, 3D ED has its unique strengths. As already exemplarily shown above, the seamless switch from diffraction to imaging mode and even coupled with spectroscopy techniques (EDXS, EELS and EFTEM) on modern TEM instruments adds valuable and manifold real space structural and chemical information to the 3D ED dataset, leading to a more comprehensive understanding of the investigated functional thin film. While 3D ED data, as demonstrated above, is of overall comparable quality to GIWAXS data (including synchrotron), it exhibits particularly high SNR in the in-plane direction, a direction which, coincidentally, is not strictly accessible with GIWAXS. Other strengths of 3D ED include the flexible camera length, which allows tuning the investigated q-range within seconds, as well as the flexible field of view, which enables to also investigate possible inhomogeneities of the thin films on a micrometer scale. With respect to future developments, 3D ED can also be applied for in situ measurements by utilizing chip-based heating devices[58,59] without compromising the accessible tilting range of the microscope holder. Depending on the required time resolution high quality data sets can be acquired for each temperature to study the temperature dependent structure. Alternatively, one could improve the time resolution towards a sub-minute regime by reducing the number of tilt angles. A recent investigation of a PM6:Y6 system has already demonstrated, that simply taking diffraction patterns under 0 and 75° provides valuable additional structural information for PM6:Y-series samples compared to relying solely on plan-view (0°) patterns.[26]

4. Conclusion and Outlook

In this work, we demonstrate 3D ED as a powerful technique to study the structure, texture, and mosaicity of beam sensitive organic polycrystalline thin films. We in particular compare 3D ED to GIWAXS as well-established technique. Here, we compare the commonalities and differences in the experimental approach, including the scattering geometry and its implications for the resulting cuts through reciprocal space. We describe the complete workflow of 3D ED, from tilt series acquisition to the 3D reconstruction of reciprocal space and the extraction of q_{rz} maps. Furthermore, we discuss the origin and implications of the missing wedges, which arise for different reasons in the q_{rz} maps of both techniques. By utilizing solvent vapor annealed DRCN5T:PC_{71}BM OSC absorber layers as model system, we qualitatively and quantitatively compare 3D ED with laboratory-based and synchrotron GIWAXS data, resulting in an excellent agreement. In conclusion, we highlight the challenges and strengths of both techniques, demonstrating not only the necessity but also the significant potential of their correlative use for a comprehensive structural thin film characterization. Looking ahead, 3D ED will benefit from the progress in detector technology in electron microscopy.[60-62] Combined with automated data acquisition procedures and data science approaches[63], these development will drastically reduce the total acquisition time and required electron dose, enabling precise structural information to be obtained with higher throughput. Furthermore, advanced structural information retrieval routines and even structural refinement methods for polycrystalline and textured samples should be developed to enhance accuracy and broaden the applicability of 3D ED.

5. Methods

Sample Preparation

The BHJ OSC samples were produced with a spin coating process. As substrates silicon wafer pieces of 1x2 cm were used due to the small surface roughness being beneficial for GIWAXS measurements (single side polished, terminated with SiO2, Siegert Wafer, Aachen, Germany). The wafer was cut to pieces which were then cleaned for 10 min in acetone and isopropanol respectively using an ultrasonic bath. On the dried substrates poly(3,4-ethylenedioxythiophene) polystyrene sulfonate (PEDOT:PSS, Clevios® P VP Al 4083, Heraeus, Hanau, Germany) in a mixture with isopropanol (ratio 1:4) was applied by doctor blading (amount of mixture 60 µl, 550 µm gap, blade speed 40 mm/s, plate temperature 50 °C). The active layer consisted of the small molecule donor DRCN5T (purity >= 99%, 1-Material, Dorval, Canada) and the

fullerene acceptor $PC_{71}BM$ (purity >=99%, Solenne BV, Groningen Netherlands) in a ratio of 1:0.8 wt.%. Both components were dissolved separately in chloroform before mixing. The solutions were prepared under inert gas atmosphere and stirred at 40°C with a speed of 150 rpm. The respective solutions were then mixed and further stirred before spin coating under inert gas atmosphere (1500 rpm). As post-processing solvent vapor annealing was applied using a closed petri dish and 120 µl of carbon disulfide. For GIWAXS measurements the samples were used prepared as described so far. For TEM the OSC thin film was detached from the silicon wafer by immersing the substrate into a petri dish filled with distilled water. Thereby the PEDOT:PSS interlayer was dissolved and the active layer floated on the water surface. The active layer was then transferred to a Ni TEM support grid (200 mesh, lacey carbon grid).

TEM and GIWAXS Characterization

TEM investigations were performed using a double-corrected Titan Themis[3] 300 (ThermoFisher Scientific) equipped with a high-brightness field-emission gun (X-FEG) and a high-resolution post-column energy filter (GIF Quantum, Gatan, Inc., Pleasanton, USA). The instrument was operated at 300 kV (λ=0.00197 nm) for both electron diffraction and STEM-EELS investigations. EF-SAED patterns were acquired with a nominal camera length of 145 mm and a 10 eV energy selecting slit around the zero-loss peak in a tilt series covering an angle range of -78° to 80° in 1° steps. Zero-loss energy filtering is necessary to suppress the inelastic scattering background at small angles, which are crucial for investigation of molecular crystallites of typically nm-sized unit cells (thus small diffraction angles). For detailed information on the influence of EF and of the contributing volume, which changes during tilting, on the detected diffracted intensity see Figure S9. Due to beam sensitivity of the sample each diffraction pattern was acquired at fresh sample areas, using a fluence of 0.45 e/$Å^2$s and 1 s acquisition time, which ensures to stay below the reported critical dose.[37] The illuminated area was 6 µm in diameter, of which an area with diameter of ~3.4 µm contributed to the ED pattern due to the SAD aperture size. The sample translation step size between ED pattern acquisitions was 10 µm. STEM-EELS data were acquired for investigation of the nanomorphology, a scanning grid of 144x144 with a probe step size of ~3 nm, a dwell time of 0.008 s and a beam current of 130 pA was used.

The laboratory GIWAXS datasets were acquired at the Versatile Advanced X-ray scattering instrument Erlangen (VAXSTER) which is equipped with a liquid metal-jet Ga source (Excillum, Kista, Sweden; Ga-K_α λ=1.341 Å) and four collimating, four-bladed slits. The Pilatus 300K detector consists of 3 modules, resulting in two stripes of missing information in the detected patterns. This can be bypassed by summing two measurements acquired with shifted detector positions (Figure S10). A sample detector distance of 178.7 mm was determined via calibration with a AgBh sample and an incidence angle of ~0.14° was

calculated using the calibrated sample-detector-distance (SDD) in combination with direct and reflected beam positions. This incidence angle is approximately the critical angle of the active layer and below the critical angle of the Si substrate ($\alpha_{c,Si}$=0.19°). The instrument was operated under vacuum conditions and the illumination time was 16 h for each pattern. The direct beam position was extracted out of a measurement with the sample removed from the beam path, for determination of the reflected beam position an additional, shorter measurement of 60 s was conducted as in the longer 16 h measurements the reflected beam pixels are saturated, which makes peak position determination challenging.

The synchrotron GIWAXS measurement was acquired at the High Resolution Diffraction Beamline P08, PETRA III, DESY.[64] The X-ray energy was 25 keV with a beam size of 0.4 x 0.1 mm, a measurement time of 10 s and an incidence angle of 0.072°. As detector a XRD 1621 flat panel (Perkin Elmer Inc., Waltham, MA, USA) was used with a SDD of 704 mm.

Data Processing and Visualization

The electron diffraction and STEM-EELS data were evaluated using Gatan Microscopy Suite (GMS3) software with public plugins and home-developed scripts. The STEM-EELS maps were computed with model-based quantification method as implemented in GMS3.

A home-made processing workflow was implemented to reconstruct the three-dimensional reciprocal space volume, based on which the q_{rz} map was calculated, for quantitative comparison with GIWAXS. The raw data is pre-processed involving the following steps:

1. Determination the center of the diffraction patterns and correct the pattern shift.
2. Determine the tilt axis by the instrumental setup and diffraction pattern symmetry considerations at the highest tilt angles.
3. Rotate the diffraction patterns so that the tilt axis coincides with the vertical image (q_y-)axis (cf. Figure below).
4. Normalize the diffraction intensity to account for different projected sample thickness and interaction volume. This is realized by normalizing to the sum intensity of the presumably isotropic $PC_{71}BM$ diffraction halo ring in each diffraction pattern (cf. Figure S9).
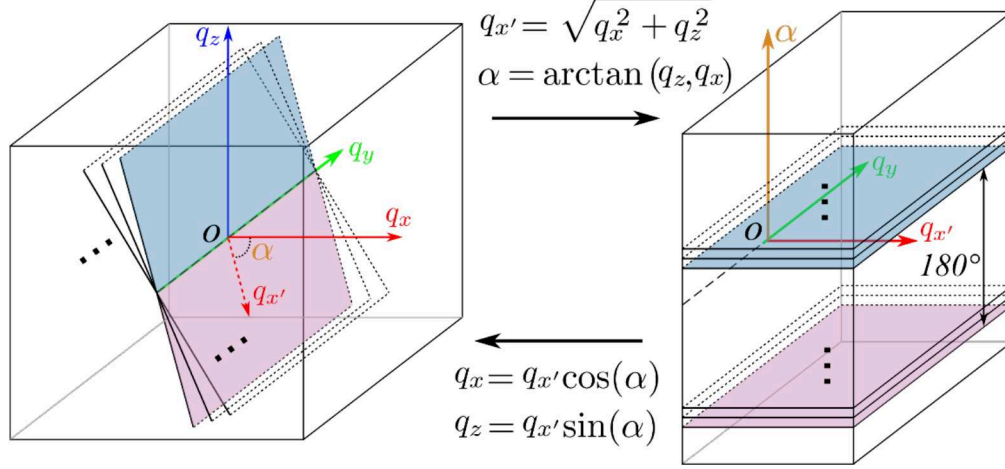
Figure 5. Reconstruction of the three-dimensional reciprocal space volume based on polar transformations.

Afterwards, the three-dimensional reciprocal space volume is reconstructed based on polar transformation as illustrated in **Figure 5** and detailed as follows. Each diffraction pattern is a slice of reciprocal space defined as in the q_{xyz} cube where q_z-axis and q_y-axis coincide with the electron travelling direction and the experimental tilt axis, respectively. Every diffraction pattern in the aligned data stack can be viewed as having a common q_y-axis, and their $q_{x'}$-axes in the patterns lie in the q_{xz} plane and are rotated by angle α (with α being zero coincident with q_x-axis and positive α in anti-clock wise direction). In the tilt series, each diffraction pattern is a slice sampling the three-dimensional reciprocal space (see **Figure 2**) with the density of sampling closer to the tilt axis higher than away from the tilt axis. We first create a new orthogonal data volume expressed in cylindrical coordinates $q_{x'}$-α-q_y and then fill the aligned raw data into this new volume. The positive side (along $q_{x'}$-axis) of each diffraction pattern fills the $q_{x'y}$ plane at α position along the α-axis, while the negative side of each diffraction pattern is filled in a plane at α position shifted by 180 degrees (along α axis). Finally, all the $q_{x'}$-α planes along the q_y-axis are transformed back to q_{xz} plane by plane according to polar transformation. In such way, we obtain the three-dimensional reciprocal space volume not only computationally efficient, but also the transformation implies an interpolation of the slice sampling at high distance to the tilt axis. The different sampling density at various distance to the tilt axis would result in increased diffraction intensities closer to the tilt axis in the reconstructed volume, which is normalized by a unit data volume of the same shape as the aligned diffraction data and reconstructed via the same scheme. In this way, the three-dimensional reciprocal space volume is reconstructed in which the scattering volume (due to thickness and projection effect) effect and sampling multiplicity are tilted, whereby the diffracted intensity can be further quantitatively evaluated. This method works very robust for datasets acquired at equal tilt increment in the experiment.

A q_{rz} map can be generated by azimuthally integrating the q_{xy} planes along q_z-axis by polar transformation of the q_{xy} planes and projection along the angle axis (see **Figure 3**b). The Friedel-pairs of diffraction intensities in the negative side along the q_z-axis are expected to be the same with the positive side. Therefore, we flip the negative side average with the positive side to further improve SNR. In this way, the q_{rz} map, similar to that of GIWAXS, is generated for quantitative comparison.

The three-dimensional reciprocal space volume is visualized using the software ChimeraX with appropriate viewing modes.[65] The ortho-plane view displayed in **Figure 3**b consists of 3 orthogonal planes of the volume with q_{xyz} as normal vectors of the planes. The videos of the volume in SI utilize a maximum intensity projection.

χ-linecuts were generated out of the 3D ED q_{rz} map by choosing ring segments of specified radial range, polar transformation and subsequent projection along the radius range. Extraction of linecuts was done using the whole available q_{rz} map information, i.e. not only one of the before mentioned data pads of negative and positive q_{rz} average. Generation of the q_{rz} map version with applied scale and color look-up-table was achieved using ImageJ[66] and a Python script based on Matplotlib[67].

For the laboratory GIWAXS data calibration of the SDD and determination of positions of direct and reflected beams by two-dimensional Gaussian fits, the software Fit2D was used.[68] Furthermore, the data were evaluated with the MATLAB based software GIXSGUI. This includes transformation into reciprocal space coordinates and extraction of different linecuts.[50] The summing of the two GIWAXS measurements with respect to the different detector positions was done using ImageJ. Peak fitting for all data shown was achieved using LIPRAS software.[69]

The synchrotron GIWAXS data were evaluated using Python-based Jupyter Notebooks[70], based on scripts provided by H.-G. Steinrück and F. Bertram. Processing included reciprocal space transformation and linecut extraction. Main python packages used were pygix[71], pyFAI[72], FabIO[73], Matplotlib[67] and NumPy[74].

Supporting Information

Supporting Information is available from the Wiley Online Library or from the author.

Acknowledgements

Conflict of interest

The authors declare no conflict of interest.

References

1   Zhu, L. *et al.* Achieving 20.8% organic solar cells via additive-assisted layer-by-layer fabrication with bulk p-i-n structure and improved optical management. *Joule* **8**, 3153-3168 (2024). https://doi.org/10.1016/j.joule.2024.08.001

2   Chen, C. *et al.* Molecular interaction induced dual fibrils towards organic solar cells with certified efficiency over 20. *Nat. Commun.* **15**, 6865 (2024). https://doi.org/10.1038/s41467-024-51359-w

3   Wang, J. *et al.* Isomerism Effect of 3D Dimeric Acceptors for Non-Halogenated Solvent-Processed Organic Solar Cells with 20 % Efficiency. *Angew Chem Int Ed Engl*, e202423562 (2024). https://doi.org/10.1002/anie.202423562

4   Yao, Z. *et al.* Complete Peripheral Fluorination of the Small-Molecule Acceptor in Organic Solar Cells Yields Efficiency over 19. *Angew Chem Int Ed Engl* **62**, e202312630 (2023). https://doi.org/10.1002/anie.202312630

5   Duan, T. *et al.* Electronic Configuration Tuning of Centrally Extended Non-Fullerene Acceptors Enabling Organic Solar Cells with Efficiency Approaching 19. *Angew Chem Int Ed Engl* **62**, e202308832 (2023). https://doi.org/10.1002/anie.202308832

6   Lu, H. *et al.* Designing A-D-A Type Fused-Ring Electron Acceptors with a Bulky 3D Substituent at the Central Donor Core to Minimize Non-Radiative Losses and Enhance Organic Solar Cell

Efficiency. *Angew Chem Int Ed Engl* **63**, e202407007 (2024).
https://doi.org/10.1002/anie.202407007

7   Osterrieder, T. *et al.* Autonomous optimization of an organic solar cell in a 4-dimensional parameter space. *Energy & Environmental Science* **16**, 3984-3993 (2023). https://doi.org/10.1039/d3ee02027d

8   Harreiß, C. *et al.* Understanding and Controlling the Evolution of Nanomorphology and Crystallinity of Organic Bulk‐Heterojunction Blends with Solvent Vapor Annealing. *Solar RRL* **6**, 2200127 (2022). https://doi.org/10.1002/solr.202200127

9   Rechberger, S. *et al.* Unraveling the Complex Nanomorphology of Ternary Organic Solar Cells with Multimodal Analytical Transmission Electron Microscopy. *Sol Rrl* **4** (2020). https://doi.org/10.1002/solr.202000114

10   Basu, R. *et al.* Large-area organic photovoltaic modules with 14.5% certified world record efficiency. *Joule* **8**, 970-978 (2024). https://doi.org/10.1016/j.joule.2024.02.016

11   Cheng, Y. *et al.* Oligomer-Assisted Photoactive Layers Enable >18 % Efficiency of Organic Solar Cells. *Angew Chem Int Ed Engl* **61**, e202200329 (2022). https://doi.org/10.1002/anie.202200329

12   Xu, J. *et al.* Doping of Mesoscopic Charge Extraction Layers Enables the Design of Long-Time Stable Organic Solar Cells. *ACS Energy Letters* **9**, 30-37 (2023). https://doi.org/10.1021/acsenergylett.3c02087

13   Liu, C. *et al.* Utilizing the unique charge extraction properties of antimony tin oxide nanoparticles for efficient and stable organic photovoltaics. *Nano Energy* **89** (2021). https://doi.org/10.1016/j.nanoen.2021.106373

14   Lüer, L. *et al.* Maximizing Performance and Stability of Organic Solar Cells at Low Driving Force for Charge Separation. *Adv Sci (Weinh)* **11**, e2305948 (2024). https://doi.org/10.1002/advs.202305948

15   Min, J. *et al.* Gaining further insight into the effects of thermal annealing and solvent vapor annealing on time morphological development and degradation in small molecule solar cells. *Journal of Materials Chemistry A* **5**, 18101-18110 (2017). https://doi.org/10.1039/c7ta04769j

16   Min, J. *et al.* High efficiency and stability small molecule solar cells developed by bulk microstructure fine-tuning. *Nano Energy* **28**, 241–249 (2016). https://doi.org/10.1016/j.nanoen.2016.08.047

17   Werzer, O. *et al.* X-ray diffraction under grazing incidence conditions. *Nature Reviews Methods Primers* **4** (2024). https://doi.org/10.1038/s43586-024-00293-8

18   Steele, J. A. *et al.* How to GIWAXS: Grazing Incidence Wide Angle X‐Ray Scattering Applied to Metal Halide Perovskite Thin Films. *Advanced Energy Materials* **13** (2023). https://doi.org/10.1002/aenm.202300760

19   Peng, Z., Ye, L. & Ade, H. Understanding, quantifying, and controlling the molecular ordering of semiconducting polymers: from novices to experts and amorphous to perfect crystals. *Mater Horiz* **9**, 577-606 (2022). https://doi.org/10.1039/d0mh00837k

20   Berlinghof, M. *et al.* Flexible sample cell for real-time GISAXS, GIWAXS and XRR: design and construction. *J Synchrotron Radiat* **25**, 1664-1672 (2018). https://doi.org/10.1107/S1600577518013218

21   Williams, D. B. & Carter, C. B. *Transmission electron microscopy: A textbook for materials science*. 2nd ed. edn, (Springer, 2009).

22   Mott, N. F. & Massey, H. S. W. *The theory of atomic collisions*. 3 edn, (Clarendon Press Oxford, 1965).

23   Du, X. *et al.* Crystallization of Sensitizers Controls Morphology and Performance in Si-/C-PCPDTBT-Sensitized P3HT:ICBA Ternary Blends. *Macromolecules* **50**, 2415-2423 (2017). https://doi.org/10.1021/acs.macromol.6b02699

24   Montenegro Benavides, C. *et al.* Improving spray coated organic photodetectors performance by using 1,8-diiodooctane as processing additive. *Organic Electronics* **54**, 21-26 (2018). https://doi.org/10.1016/j.orgel.2017.12.022

25   Sun, R. *et al.* 18.2%-efficient ternary all-polymer organic solar cells with improved stability enabled by a chlorinated guest polymer acceptor. *Joule* **7**, 221-237 (2023). https://doi.org/10.1016/j.joule.2022.12.007

26   Fürk, P. *et al.* The challenge with high permittivity acceptors in organic solar cells: a case study with Y-series derivatives. *Journal of Materials Chemistry C* **11**, 8393–8404 (2023). https://doi.org/10.1039/d3tc01112g

27   Gasparini, N. *et al.* Designing ternary blend bulk heterojunction solar cells with reduced carrier recombination and a fill factor of 77%. *Nature Energy* **1**, 16118 (2016). https://doi.org/10.1038/nenergy.2016.118

28   Kolb, U., Gorelik, T. & Otten, M. T. Towards automated diffraction tomography. Part II--Cell parameter determination. *Ultramicroscopy* **108**, 763-772 (2008). https://doi.org/10.1016/j.ultramic.2007.12.002

29   Kolb, U., Gorelik, T., Kübel, C., Otten, M. T. & Hubert, D. Towards automated diffraction tomography: part I--data acquisition. *Ultramicroscopy* **107**, 507–513 (2007). https://doi.org/10.1016/j.ultramic.2006.10.007

30   Zhang, D., Oleynikov, P., Hovmöller, S. & Zou, X. Collecting 3D electron diffraction data by the rotation method. *Zeitschrift für Kristallographie* **225**, 94-102 (2010). https://doi.org/10.1524/zkri.2010.1202

31   Wan, W., Sun, J., Su, J., Hovmoller, S. & Zou, X. Three-dimensional rotation electron diffraction: software RED for automated data collection and data processing. *J. Appl. Crystallogr.* **46**, 1863-1873 (2013). https://doi.org/10.1107/S0021889813027714

32   Yuan, S. *et al.* [Ti(8)Zr(2)O(12)(COO)(16)] Cluster: An Ideal Inorganic Building Unit for Photoactive Metal-Organic Frameworks. *ACS Cent Sci* **4**, 105-111 (2018). https://doi.org/10.1021/acscentsci.7b00497

33   Burla, M. C. *et al.* Crystal structure determination and refinementviaSIR2014. *J. Appl. Crystallogr.* **48**, 306-309 (2015). https://doi.org/10.1107/s1600576715001132

34   Palatinus, L. & Chapuis, G. SUPERFLIP– a computer program for the solution of crystal structures by charge flipping in arbitrary dimensions. *J. Appl. Crystallogr.* **40**, 786-790 (2007). https://doi.org/10.1107/s0021889807029238

35   Sheldrick, G. M. A short history of SHELX. *Acta Crystallogr A* **64**, 112-122 (2008). https://doi.org/10.1107/S0108767307043930

36   Gemmi, M. *et al.* 3D Electron Diffraction: The Nanocrystallography Revolution. *ACS central science* **5**, 1315–1329 (2019). https://doi.org/10.1021/acscentsci.9b00394

37   Wu, M. *et al.* Seeing structural evolution of organic molecular nano-crystallites using 4D scanning confocal electron diffraction (4D-SCED). *Nature communications* **13**, 2911 (2022). https://doi.org/10.1038/s41467-022-30413-5

38   Berlinghof, M. *et al.* Crystal-structure of active layers of small molecule organic photovoltaics before and after solvent vapor annealing. *Zeitschrift für Kristallographie - Crystalline Materials* **235**, 15–28 (2020). https://doi.org/10.1515/zkri-2019-0055

39   Savikhin, V. *et al.* GIWAXS-SIIRkit: scattering intensity, indexing and refraction calculation toolkit for grazing-incidence wide-angle X-ray scattering of organic materials. *Journal of Applied Crystallography* **53**, 1108-1129 (2020). https://doi.org/10.1107/s1600576720005476

40   Smilgies, D. M. Scherrer grain-size analysis adapted to grazing-incidence scattering with area detectors. *J. Appl. Crystallogr.* **42**, 1030-1034 (2009). https://doi.org/10.1107/S0021889809040126

41 Müller-Buschbaum, P. The active layer morphology of organic solar cells probed with grazing incidence scattering techniques. *Advanced materials (Deerfield Beach, Fla.)* **26**, 7692–7709 (2014). https://doi.org/10.1002/adma.201304187

42 Gemmi, M. & Lanza, A. E. 3D electron diffraction techniques. *Acta crystallographica Section B, Structural science, crystal engineering and materials* **75**, 495–504 (2019). https://doi.org/10.1107/s2052520619007510

43 De Graef, M. *Introduction to Conventional Transmission Electron Microscopy*. (Cambridge University Press, 2003).

44 De Graef, M. & McHenry, M. E. *Structure of materials: An introduction to crystallography, diffraction, and symmetry / Marc De Graef, Carnegie Mellon University, Pittsburgh, Michael E. McHenry, Carnegie Mellon University, Pittsburgh*. Second edition, fully revised and updated. edn, (Cambridge University Press, 2012).

45 Fultz, B. & Howe, J. *Transmission electron microscopy and diffractometry of materials*. 3 edn, (Springer-Verlag, 2008).

46 Kolb, U., Krysiak, Y. & Plana-Ruiz, S. Automated electron diffraction tomography - development and applications. *Acta Crystallogr B Struct Sci Cryst Eng Mater* **75**, 463-474 (2019). https://doi.org/10.1107/S2052520619006711

47 Gasser, F. *et al.* Intensity corrections for grazing-incidence X-ray diffraction of thin films using static area detectors. *J. Appl. Crystallogr.* **58**, 96-106 (2025). https://doi.org/10.1107/S1600576724010628

48 Baker, J. L. *et al.* Quantification of thin film crystallographic orientation using X-ray diffraction with an area detector. *Langmuir : the ACS journal of surfaces and colloids* **26**, 9146–9151 (2010). https://doi.org/10.1021/la904840q

49 Rivnay, J., Mannsfeld, S. C. B., Miller, C. E., Salleo, A. & Toney, M. F. Quantitative determination of organic semiconductor microstructure from the molecular to device scale. *Chemical reviews* **112**, 5488–5519 (2012). https://doi.org/10.1021/cr3001109

50 Jiang, Z. GIXSGUI : a MATLAB toolbox for grazing-incidence X-ray scattering data visualization and reduction, and indexing of buried three-dimensional periodic nanostructured films. *Journal of Applied Crystallography* **48**, 917–926 (2015). https://doi.org/10.1107/s1600576715004434

51 Dippel, A. C. *et al.* Local atomic structure of thin and ultrathin films via rapid high-energy X-ray total scattering at grazing incidence. *IUCrJ* **6**, 290-298 (2019). https://doi.org/10.1107/S2052252519000514

52 Qin, M., Chan, P. F. & Lu, X. A Systematic Review of Metal Halide Perovskite Crystallization and Film Formation Mechanism Unveiled by In Situ GIWAXS. *Adv. Mater.* **33**, e2105290 (2021). https://doi.org/10.1002/adma.202105290

53 Yoshioka, C., Carragher, B. & Potter, C. S. Cryomesh: a new substrate for cryo-electron microscopy. *Microsc. Microanal.* **16**, 43-53 (2010). https://doi.org/10.1017/S1431927609991310

54 Quispe, J. *et al.* An improved holey carbon film for cryo-electron microscopy. *Microsc. Microanal.* **13**, 365-371 (2007). https://doi.org/10.1017/S1431927607070791

55 Rivnay, J. *et al.* Drastic Control of Texture in a High Performance n-Type Polymeric Semiconductor and Implications for Charge Transport. *Macromolecules* **44**, 5246-5255 (2011). https://doi.org/10.1021/ma200864s

56 Klein, H., Yoruk, E. & Kodjikian, S. Structure solution and refinement of beam-sensitive nano-crystals. *Micron* **181**, 103634 (2024). https://doi.org/10.1016/j.micron.2024.103634

57 Mugnaioli, E. *et al.* Electron Diffraction on Flash-Frozen Cowlesite Reveals the Structure of the First Two-Dimensional Natural Zeolite. *ACS Cent Sci* **6**, 1578-1586 (2020). https://doi.org/10.1021/acscentsci.9b01100

58	Adegoke, T. E. *et al.* Real-Time TEM Observation of the Role of Defects on Nickel Silicide Propagation in Silicon Nanowires. *ACS Nano* **18**, 10270-10278 (2024). https://doi.org/10.1021/acsnano.4c01060

59	Niekiel, F., Kraschewski, S. M., Schweizer, P., Butz, B. & Spiecker, E. Texture evolution and microstructural changes during solid-state dewetting: A correlative study by complementary in situ TEM techniques. *Acta Mater* **115**, 230–241 (2016). https://doi.org/10.1016/j.actamat.2016.05.026

60	Levin, B. D. A. Direct detectors and their applications in electron microscopy for materials science. *Journal of Physics: Materials* **4** (2021). https://doi.org/10.1088/2515-7639/ac0ff9

61	Hattne, J., Clabbers, M. T. B., Martynowycz, M. W. & Gonen, T. Electron counting with direct electron detectors in MicroED. *Structure* **31**, 1504-1509 e1501 (2023). https://doi.org/10.1016/j.str.2023.10.011

62	Wu, M., Stroppa, D. G., Pelz, P. & Spiecker, E. Using a fast hybrid pixel detector for dose-efficient diffraction imaging beam-sensitive organic molecular thin films. *Journal of Physics: Materials* **6** (2023). https://doi.org/10.1088/2515-7639/acf524

63	Spurgeon, S. R. *et al.* Towards data-driven next-generation transmission electron microscopy. *Nat Mater* **20**, 274-279 (2021). https://doi.org/10.1038/s41563-020-00833-z

64	Seeck, O. H. *et al.* The high-resolution diffraction beamline P08 at PETRA III. *J Synchrotron Radiat* **19**, 30-38 (2012). https://doi.org/10.1107/S0909049511047236

65	Pettersen, E. F. *et al.* UCSF ChimeraX: Structure visualization for researchers, educators, and developers. *Protein science : a publication of the Protein Society* **30**, 70–82 (2021). https://doi.org/10.1002/pro.3943

66	Schindelin, J. *et al.* Fiji: an open-source platform for biological-image analysis. *Nature methods* **9**, 676–682 (2012). https://doi.org/10.1038/nmeth.2019

67	Hunter, J. D. Matplotlib: A 2D Graphics Environment. *Computing in Science and Engineering* **9**, 90-95 (2007). https://doi.org/10.1109/MCSE.2007.55

68	Hammersley, A. P. FIT2D: a multi-purpose data reduction, analysis and visualization program. *Journal of Applied Crystallography* **49**, 646-652 (2016). https://doi.org/10.1107/s1600576716000455

69	Esteves, G., Ramos, K., Fancher, C. M. & Jones, J. L. *LIPRAS: Line-Profile Analysis Software* (2017).

70	Kluyver, T. *et al.* (IOS Press, 2016).

71	pygix.

72	Kieffer, J. & Karkoulis, D. PyFAI, a versatile library for azimuthal regrouping. *Journal of Physics: Conference Series* **425**, 202012 (2013). https://doi.org/10.1088/1742-6596/425/20/202012

73	Knudsen, E. B., Sørensen, H. O., Wright, J. P., Goret, G. & Kieffer, J. FabIO: easy access to two-dimensional X-ray detector images in Python. *J. Appl. Crystallogr.* **46**, 537-539 (2013). https://doi.org/10.1107/s0021889813000150

74	van der Walt, S., Colbert, S. C. & Varoquaux, G. The NumPy Array: A Structure for Efficient Numerical Computation. *Computing in Science and Engineering* **13**, 22-30 (2011). https://doi.org/10.1109/MCSE.2011.37